RheoTack - An approach to investigate retraction rate dependent detaching behavior of pressure sensitive adhesives

RheoTack evaluation of detaching behavior of silicone-based pressure sensitive adhesives for transdermal therapeutic systems

Michael Meurer[a,b], Gatien Kamsu Fogain[a], Esther Ramakers-van Dorp[a], Christian Dresbach[a], Bernhard. Möginger[a], Berenika Hausnerova[b,c,*]

[a]*Department of Natural Sciences, Bonn-Rhein-Sieg University of Applied Sciences, 53359, Germany*

[b]*Department of Production Engineering Tomas Bata University in Zlin, 76001, Czech Republic*

[c]*Centre of Polymer Systems, Tomas Bata University in Zlín 76001 Zlín, Czech Republic*

[*]*Corresponding author at: Department of Production Engineering, Tomas Bata University in Zlin, 76001, Czech Republic. E-mail address: hausnerova@utb.cz (B. Hausnerova).*

ABSTRACT

This study focuses on applying the RheoTack method to assess the detaching behavior of transdermal therapeutic systems (TTS), which represent skin-applied medications comprising a drug-loaded pressure-sensitive adhesive (PSA) and a flexible backing layer. The RheoTack method provides detailed force-retraction displacement-curves ($F-h$-curves) that reveal the influence of chemical structure and resin content on PSA deformation and fibril formation. To compare various rod geometries (flat rods with diameters of 5 mm and 8 mm, and a spherically rounded rod with a contact area of 5 mm^2), the force-retraction displacement curves were normalized to account for the effective contact areas. The flat and spherical rods led to completely different $F-h$-curves as well as different failure and tack behaviors. Furthermore, the adhesion formation between the TTS with flexible backing layers and rods during the dwell phase occurs in a different manner compared with rigid plates, particularly for flat rods, where maximum compression stresses occur at the edges and not uniformly over the cross-section. Measurements of $F-h$-curves were performed with retraction speeds of 0.01, 0.1, and 1 mm/s. The increase in retraction speed increased the stiffness from 250 to 1200 N/m for non-amine-compatible PSA measured with a rod of 8 mm. RheoTack measurements were performed with a dwell time of 1 s, which is consistent with ASTM D2949. However, the TTS was in the adhesion-establishing compression phase for 3 s at 1 mm/s and for 30 s at 0.01 mm/s. Thus, the approach to follow $ASTM$ D2949 has to be reconsidered for testing TTS materials.

Keywords: Transdermal therapeutic systems, pressure sensitive adhesive, detaching Rod geometry, retraction speed

1. Introduction

Transdermal therapeutic systems (TTS) are modern medication treatments for severe pain, Parkinson's disease, and Alzheimer's disease. TTS can be divided into matrix- and reservoir-type

systems [**1**]. The matrix type (**Fig. 1**) consists of a drug-in-adhesive polymer matrix positioned between a flexible protective backing layer and release liner [**2,3**]. The reservoir type features a protective backing layer, liquid or gel-like drug reservoir, semi-permeable, rate-controlling membrane, and contact adhesive layer [**1**].

Polymer-based pressure-sensitive adhesives ($PSAs$) are commonly used because they adhere well to the human skin with minimal pressure and can be removed without leaving any residue. During the application period of a few hours to seven days [**2-4**], they release a continuous, low-concentration drug flux through the skin [**5**]. These conditions pose a significant challenge for $PSAs$ as they must also resist sweat, cutaneous sebum, and daily skin movements.

The outer layer of a TTS is a thin, flexible, and protective backing film composed of polyethylene, polyvinyl chloride, polyethylene tere-phthalate, polyurethane, or elastomers, which prevents undesired contact with the drug and enhances drug permeation by reducing sweat evaporation through its occlusive properties [**3,6**]. The drugs are either embedded in a reservoir patch as a solution, suspension, or gel on a semipermeable membrane, or dissolved in the PSA of the matrix-type TTS [**1,3**]. Drugs formulated for patch delivery typically have molecular weights $<$ 500 Da and melting points $<$ 250 °C. Currently, 20-30 drug molecules are commercially available [**2,3,6**]. The semi-permeable membrane controls drug release through the adhesive contact layer and skin [**6**].

Typical skin-contact $PSAs$ used for TTS include acrylates, polyisobutylenes, and silicones. Additionally, PSA should minimize skin irritation, and easy trauma-free removal is essential [**2**]. Silicones, in particular, exhibit low toxicity, low chemical reactivity with both drugs and skin, and strong adhesion to low-surface-energy materials such as human skin [**7**].

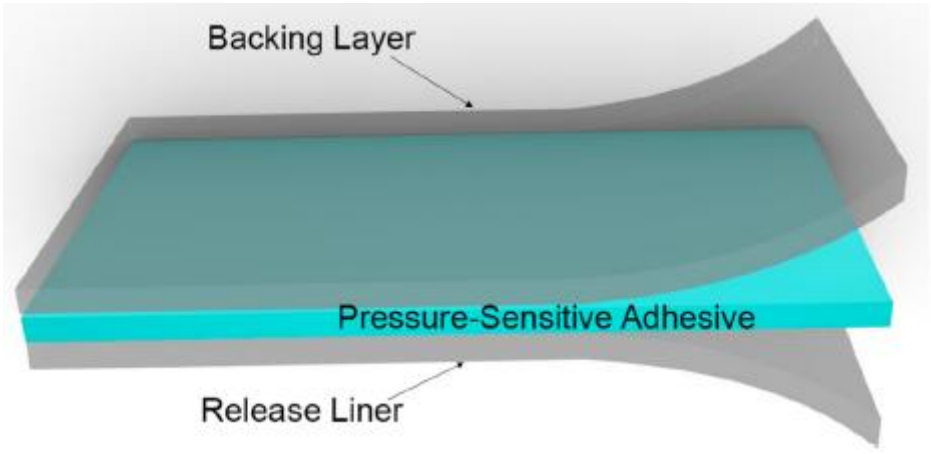

Fig. 1. Structure of a Transdermal Therapeutic System (TTS).

Silicone-based PSA consists of a viscoelastic polymer fluid and a solid-like resin component cross-linked in a “bodying process” via a polycondensation reaction [**4,7,8**]. The chosen resin content has significant effects on the viscoelastic properties in terms of the complex moduli [**4,9,10**], complex viscosity, flowability, and wettability. A higher resin content reduces the flow of PSA molecules into pores and the roughness of the skin surface, leading to a smaller contact area, less mechanical anchoring of the molecules, and less adhesion. Fang and Karyu reported that an increasing cross-linking degree within acrylic latexes and copolymers causes a decrease in deformation and flow-ability, resulting in weakened bonding to the substrate and, therefore, lower tack values [**11,12**].

A decrease in resin content increases the tack values in terms of the maximum force or stress of silicone-based PSA [**13**] and acrylate-based PSA [**14**]. Lindner et al. [**15**] reported a similar behavior for a model acrylic PSA, found an increase in the maximum force or stress values when the co-monomer content of acrylic acid was increased from 2 to 8 %. For a rubber stybelite ester-based PSA, Hammond [**16**] measured larger probe tack values when the resin content was reduced from 90 to 0 %. Thus, the flow and tack properties of PSA can be tailored by adding a softener (reduction in viscosity) or filler-like resin (increase in viscosity) to meet the requirements of a given application. The increase in both stiffness and viscosity can be explained by the reinforcing effect of fillers having a larger stiffness than that of the polymer [**17**]. Second, the resin can increase the cross-linking density of PSA via further chemical reactions, leading to higher molecular weights [**13**].

In addition to the PSA composition, the testing conditions also affected the tack behavior. Owing to the viscoelastic nature of PSA, an increasing retraction speed leads to the stiffening of acrylate-based and silicone-based PSA [**14,18-20**]. At high retraction speeds, the tack values were small and reached a maximum at low retraction speeds because the recoiling and relaxation of macromolecules dominated the deformation-induced orientation. The increase in compression and dwell times establishes better adhesion of the PSA to substrates or rods [**21**]. The tack values increase until they reach the PSA substrate-specific tack maximum [**22,23**].

Previous tack evaluation methods were conducted using custom-designed setups [**14,24-26**], commercial texture analyzers [**27**], and rheometers [**28-32**]. The testing procedures used in these studies did not comply with $ASTM$ D2979 [**33**] and varied in contact speed, contact pressure, dwell time, and retraction speed.

Additionally, these methods utilize non-deformable supports (e.g., glass or metal plates) to measure force-displacement curves and observe cavitation and fibrillation during detachment [**14,24,25**]. While all the previously mentioned testing methods record force-displacement curves [**14,24-27,29-32**], this represents an improvement compared to the single-point measurement defined in $ASTM$ D2979 [**33**]. Flexible or soft supports, such as the backing layer of a TTS, have not been taken into account so far.

Both spherical [**18,20,23,34-36**] and flat rods [**12,14,19,21,37-39**] have been used in tack experiments. The shape of a spherical rod causes good alignment to the adhesive surface, which leads to well-defined crack propagation during detaching, although this geometry induces a non-uniform stress field in the bulk [**20,40**]. Creton and Cicotti [**40**] reported that spherical rods are more widespread in the adhesion testing of non-fibrillating rubbers, where the plastic region at a crack tip is much smaller than the contact radius of the rod. Flat rods are used for highly viscoelastic and soft adhesives, where the peeling of an adhesive strip is much larger than the adhesive layer itself and is not an intrinsic property of the fracture surface or interface [**40**]. Flat rods establish an almost uniform stress field in the adhesive layer, easing the analysis, but are sensitive to slight differences in the bulk or interfacial properties [**16,18,29**].

If the radius of a spherical indenter is large compared to the thickness of the adhesive layer, detachment occurs under tension across the contact area, and the entire thickness of the PSA layer contributes to detachment [**34**]. Creton and Lakrout [**41**] as well as Takahashi et al. [**18**] used rigid metal or glass plates as substrates.

Depending on the chosen parameters (temperature, retraction speed, resin content, etc.), several researchers [**14,15,18,19,27,42,43**] have reported the occurrence of cavitation and fibrillation during tack tests as a phenomenon similar to crazing in glassy polymers. Deblieck et al. [**44**] reported that crazing in glassy polymers is initiated by the formation of microvoids or cavitation at local stress concentrations owing to heterogeneities in the molecular network. A further increase in the applied

stress leads to the growth of microvoids perpendicular to the first principal stress, which can be temporarily stopped by fibril formation. Estevez et al. [**45**] reported that a plastic zone develops at the crack tips during the growth of a void to a craze-providing material because of the shear flow to form fibrils and enable their length growth. This stabilizes the lateral size of the craze as the external deformation is compensated for by fibril growth and elongation. At slow deformation rates, fibrils can elongate more because of the lower flow resistance and orderly alignment of macromolecules [**46**]. With increasing deformation rate, fibril elongation is limited because of the strain hardening of the fibrils until fibril fracture occurs [**37**]. At high deformation rates, the process of fibril formation cannot be initiated, and microvoid formation immediately leads to unstable crack growth. Furthermore, Basu et al. [**47**] used the entanglement density (or cross-linking density) in a polymer as a measure of the maximum stretchability of the fibrils. A lower entanglement density makes a polymer more prone to crazing, with longer and slender fibrils.

The scope of this study was to investigate the effects of PSA composition in terms of chemical structure and resin content, as well as the effects of rod geometry on establishing adhesion under compression during dwell time. The retraction speed-dependent detaching behavior of TTS using the RheoTack method [**19**] provides much more information about the established adhesion states in terms of force-retraction displacement-curves and visual observation of the deformation structures compared to the tack test according to $ASTM$ D2979. Thus, the scope of this study was to investigate the effects of PSA composition in terms of chemical structure and resin content, as well as the effects of rod geometry on the detaching behavior to ease the development of tailormade TTS.

2. Experimental

2.1. Materials

Four commercially available silicone-based $PSA - BIO - PSA$ 7-4201 (Biomedical Pressure-Sensitive Adhesive, medium tack), $BIO - PSA$ 7-4301 (high tack), $BIO - PSA$ 7-4501 (medium tack), $BIO - PSA$ 7-4601 (high tack) - were supplied by DuPont and Dow Healthcare Solutions, all with a branched structure [**48-51**]. These $BIO - PSAs$ were mixed at different ratios to produce 3 amine-compatible (AC) PSA and 3 nonamine-compatible (NAC) PSA with different resin contents, v_F and chemical structures (**Table 1**). $NAC\ PSA$ has functional OH end groups, whereas AC-PSA has functional CH_3-end groups.

From these six compounds, placebo transdermal therapeutic systems (TTS with a thickness of 150 μm $\pm$ 15 μm) were manufactured in a coating box on a release liner and laminated with a transparent poly-ester/ethylene-vinyl acetate backing layer (3 M ScotchpackTM 9732) [**52**] with a thickness of 50 μm $\pm$ 2 μm, longitudinal storage modulus of 3807 $\pm$ 55 MPa, and transversal storage modulus of 4592 $\pm$ 95 MPa. The storage moduli of the backing layer were measured using dynamic mechanical analysis (DMA Artemis E, NETZSCH, Selb, Germany) in the tension mode at 30 °C with an amplitude of 25 μm at a frequency of 1 Hz. As the backing layer is provided as a roll, the sample “longitudinal” is prepared in roll direction, whereas “transversal” indicates that the sample preparation is rectangular in the roll direction.

2.2. Methods

RheoTack measurements were performed at room temperature using a rheometer (Haake MARS III, Thermo Fisher Scientific, Waltham, MA, USA) with three differently positioned synchronized cameras

as optical observation units and an exchangeable temperature module plate (TMP) as a sample holder (Thermo Electron, Karlsruhe, Germany). In principle, RheoTack can be implemented in all commercially available rotational rheometers, which allows the measurement of normal forces. The measurements were performed six times in the following manner.

- The samples were punched out from a TTS sheet with a diameter of 20 mm. After removing the release liner, the PSA with the backing layers was fixed in a TMP with an inner diameter of 12 mm. Then, it was mounted on the rheometer with the PSA side pointing toward the rod.
- Then, the rod is moved towards the PSA to establish contact with a compression force of 0.2 N for a dwell time of 1 s.
- The retraction experiment started with retraction speeds vretmct of 0.01, 0.1, and 1 mm/s, and force-retraction displacement curves were recorded. Assuming homogeneous deformation of a 150 μm thick PSA film yields strain rates of 0.067, 0.67 and 6.7 1/s.
- All diagrams were rescaled with respect to retraction displacement to confirm that $h = 0$ coincided with $F = 0$ in the retraction curve.

Three rod geometries were chosen (**Table 2**) to investigate their effects on the detaching behavior. Surface roughness was measured using a digital microscope (Keyence VHX-7000, Keyence, Osaka, Japan). The rod geometries lead to different contact areas between the PSA and rod, and consequently, different measured forces.

Chiche et al. [**43**] found that the surface roughness Ra strongly affects the debonding stresses of acrylic-based PSA as long as Ra remains smaller than 0.060 μm. At larger Ra values, the debonding stresses became constant. As the surface roughness of $P5$, $P8$ and $R5$ range between 0.24 and 0.75 μm, **Table 2**, their roughness is clearly above 0.060 μm allowing for comparison.

Table 1 Composition of PSA having different resin contents.

Amine compatible (AC-TTS)			Non-amine compatible (NAC-TTS)		
Ratio BIO PSA 7–4201: 7–4301	Weight Content (%)	Volume Content (%)	Ratio BIO PSA 7–4501: 7–4601	Weight Content (%)	Volume Content (%)
100:0	60.00	54.2	100:0	60.00	54.2
50:50	57.50	51.6	50:50	57.50	51.6
0:100	55.00	49.1	0:100	55.00	49.1

Table 2 Rod geometries - dimensions and surface roughness; grid distance is 5 mm.

Code	Rod geometry		Diameter D (mm)	Surface roughness Ra (µm)
P8	Flat cylinder, large $A_{contact} \cong 50mm^2$		8	0.43 ± 0.11
P5	Flat cylinder, small $A_{contact} \cong 20mm^2$		5	0.75 ± 0.41
R5	Spherically rounded rod $A_{contact} \approx 5-10mm^2$		5	0.24 ± 0.03

A compression force of 0.2 N was applied in accordance with $ASTM$ D2979 [**33**]. However, the compression stresses generated by the rods during the dwell phase varied because of the different contact areas: 4 kPa ($P8$), 10 kPa ($P5$), and 64 kPa ($R5$). This leads to different adhesion states as well as different displacements at the end of the dwell time hdwell because of the mechanical properties of the TTS (PSA and backing layer), **Table 3**. The increase in the PSA shear moduli with resin content leads to a decrease in hdwell.

The use of rods with diameters of 8 mm and 5 mm leads to gaps between the TMP and rods of 2 mm and 3.5 mm, respectively, which changes the geometry of the experimental conditions, as shown by the different inclination angles of the TTS in the gap in **Fig. 2**.

In **Fig. 3**, a force-retraction displacement-curve is shown to illustrate the determination of all evaluated RheoTack parameters: PSA stiffness S, force at beginning fibril formation $F_{start\ fib}$, retraction displacement at beginning fibril formation $h_{start\ fib}$, activation energy of fibril formation $E_{start\ fib}$, maximum force F_{max} and retraction displacement at maximum force h_{max}, and adhesion energy E_{adh}. RheoTack parameters were determined for each force-retraction displacement curve to calculate the mean values and standard deviations (STD). In the diagrams, the data are shown as mean curves and the error bars represent the scatter among the measurements.

Plate-plate-oscillatory shear tests were performed on a Haake MARS III, Thermo Fisher Scientific, Waltham, MA, USA) in controlled strain mode to determine storage moduli G', loss moduli G'' and loss factor tan (δ) of the PSA between — 5 °C and 80 °C. As the RheoTack measurements were performed at 23 ° C, it is relevant to interpret the composition dependent effects on the temperature difference

on the maxima of G'' and tan(δ). Samples with a diameter of 20 mm were punched out from the PSA produced between the two release liners.

Table 3 Resin content dependent storage moduli G' and displacements at the end of the dwell time h_{dwell} of $AC-TTS$ and $NAC-TTS$.

PSA type	Resin content	h_{dwell} (P8)	h_{dwell} (P5)	h_{dwell} (R5)	G' (1 Hz)
	%	µm	µm	µm	kPa
AC	49.1	209 ± 31	318 ± 25	436 ± 35	330
	51.6	172 ± 18	250 ± 23	381 ± 26	1,950
	54.2	124 ± 20	234 ± 20	345 ± 16	4,300
NAC	49.1	205 ± 28	320 ± 20	435 ± 24	120
	51.6	186 ± 20	289 ± 17	408 ± 15	570
	54.2	164 ± 14	246 ± 16	374 ± 25	2,000

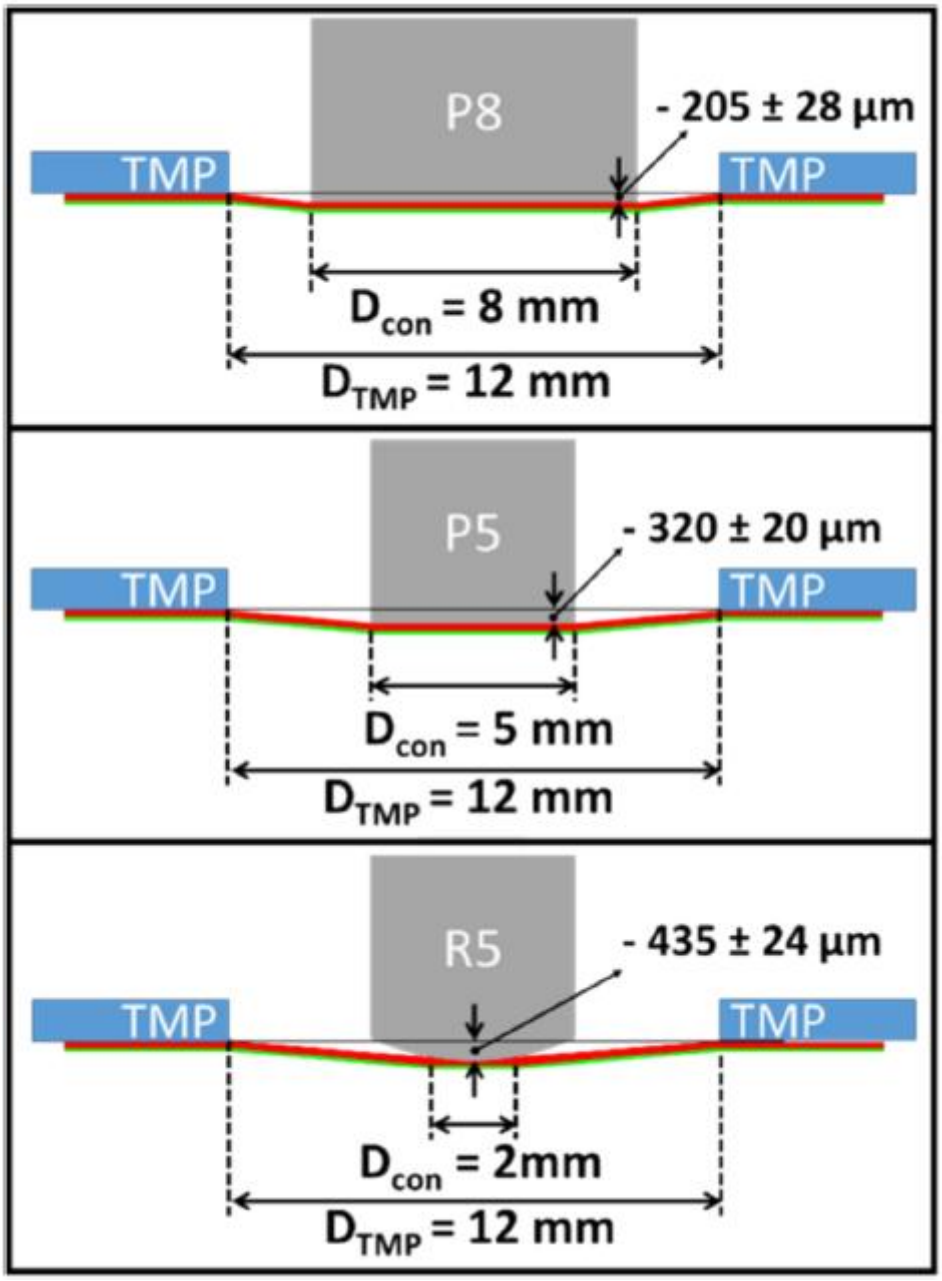

Fig. 2. Initial geometrical situations of the rods $P8$, $P5$, and $R5$ with displacements at the end of the dwell time and corresponding inclination angles of the TTS in the gap for $NAC - TTS$ with $v_F = 49.1$ %.

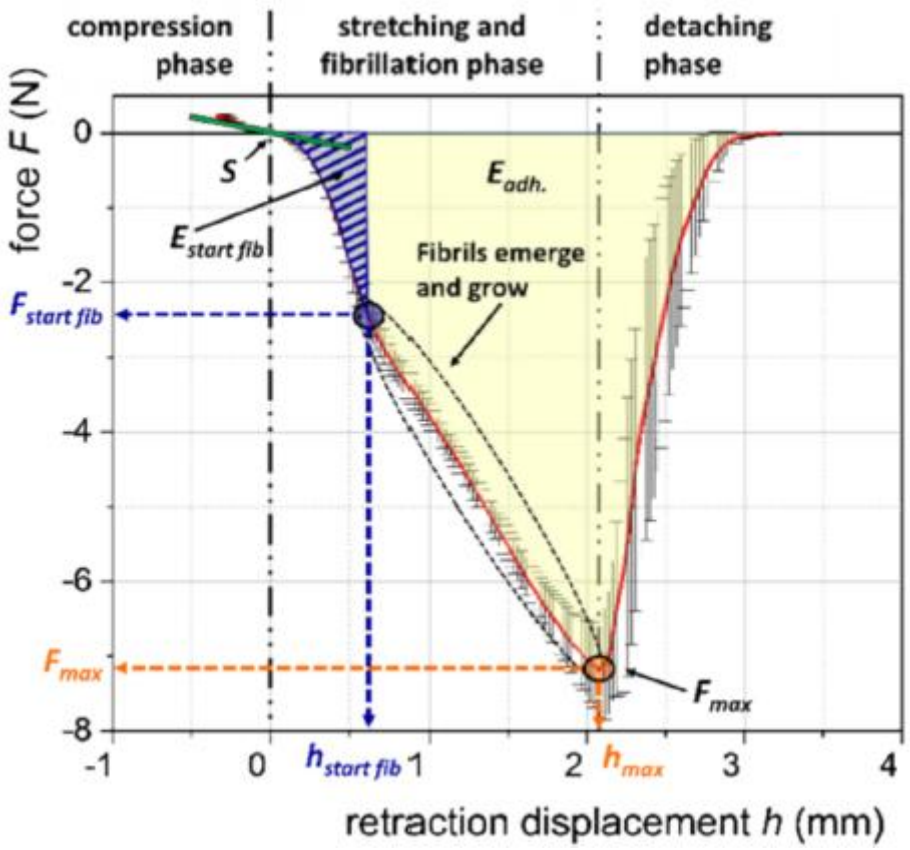

Fig. 3. Example of a force-retraction displacement-curve with the indication of deformation phases and RheoTack parameters.

To achieve a thickness of approximately 450 μm, three PSA layers were piled onto the lower plate at room temperature after removing the release liners. To confirm good adhesion between layers and plates, the sample was compressed with an axial force of 5 N for 15 s. Then, the axial force was set to zero, the sample was cooled to the starting temperature of — 5 °C and settled for of 5 min. PSA was heated to 80 °C at a rate of 2 K/min, a strain amplitude of 1 %, and a frequency of 1 Hz.

3. Results and discussion

Both the chemical structure and resin content significantly affected the force-retraction displacement-curves ($F-h$ curves) of the RheoTack measurements. $AC-TTS$ with CH_3-endgroups has a smaller maximum force F_{max} and adhesion energy E_{adh} than the corresponding $NAC-TTS$ with OH end groups, **Fig. 4**. For $AC-PSA$, the F_{max} is increased from 0.4 to 5 N, and E_{adh} is increased from 74 to 4600 μJ, whereas for $NAC-PSA$ F_{max} is increased from 1.3 to 7.3 N and $E_{adh}$from 340 to 10,200 μJ, respectively. Thus, $NAC-PSA$ is more effective than $AC-PSA$ for a given resin content and exhibits better flow and wetting behavior on metal surfaces. The macromolecules of $NAC-PSA$ flow faster in the pores and surface roughness, providing more contact area during dwell time. Furthermore, the OH end groups of $NAC-PSA$ establish more polar interactions with metal substrates, which increases the adhesion energy.

The retraction displacement at maximum force h_{max} of $AC-PSA$ are increased from 0.2 to 1 mm and of $NAC-PSA$ from 0.4 to 2.1 mm, respectively. This indicates that decreasing the resin content shifts the start of fibril fracture to larger deformations and significantly enhances fibril stretchability.

With increasing resin content, S of $AC-PSA$ is increased from 0.4 to 1.3 N/mm, and for $NAC-PSA$ S is only moderately increased from 0.4 N/mm to 0.6 N/mm, **Table 4** and **Fig. 5**. Below a resin content of 50 %, both PSA had identical stiffness within the accuracy of the measurements. Furthermore, this resin content dependency indicates the presence of a transition towards more solid-like behavior above v_F = 51 % for $AC-PSA$ and above $v_F = 54$ % for NAC-PSA, **Fig. 5**. Because of the viscoelastic character of PSA, one can expect that this transition behavior shifts to smaller resin contents for larger retraction speeds.

All $F-h$-curves show little scatter in the compression phase, as well as in the stretching and fibrillation phases prior to F_{max}. In the detaching phase, after exceeding F_{max}, the first fibrils break, and with ongoing retraction, the rate of fibril fracture increases and the force decreases. Because fibril fracturing is a stochastic process, the scatter in the $F-h$-curves increases significantly.

The chosen rod geometry significantly affects the retraction speed dependent $F-h$-curves of all PSA, **Figs. 6 and 7**. Qualitatively, the shapes of the $F-h$-curves of a given PSA are identical for $P5$ and $P8$ at the three retraction speeds but differ in the tack-relevant properties, such as F_{max} and E_{adh} in the range of 200 % to 500 %, and not around 250 %, as expected from the ratios of the cross-sections. Thus, the deviations must be attributed to the differences in the adhesion states resulting from the geometrical conditions, **Fig. 2**. The corresponding effects on fibril formation and detachment processes, depending on the PSA composition, are considered later in more detail.

At retraction speeds of 1 mm/min with $P5$, $AC-PSA$ with resin contents of 51.6 % and 54.2 %, as well as $NAC-PSA$ with a resin content of 54.2 %, established such low adhesions that they detached immediately when undergoing tensile loading. For $P8$, this behavior was only observed for $AC-PSA$ with a resin content of 54.2 %. Thus, the determination of the tack properties is limited to lower resin contents if $P5$ and $P8$ are used at a retraction speed of 1 mm/min.

With increasing resin content, S of $AC-PSA$ measured with P5 and P8 are increased by a factor 4 to 5, whereas $F_{start\,\mathrm{fib}}$, $h_{start\,\mathrm{fib}}$, $E_{start\,\mathrm{fib}}$, and h_{max} are decreased to 1/4 or 1/5. A much higher decrease to 1/10 or 1/ 100 is observed for tack-relevant quantities, such as F_{max} and E_{adh}., **Tables 4 and 5**. The decrease of RheoTack parameters of $NAC-PSA$ differs to those of $AC-PSA$ as $h_{start\,fib}$ and h_{max} are decreased to 1/4 or 1/5, whereas $F_{start\,fib}$, $E_{start\,fib}$, and the tack-relevant quantities as F_{max} and E_{adh}. decreased to 1/5 or 1/50, **Tables 4 and 5**. This shows that the PSA properties change significantly if the resin content is varied in the range of 49.1 % to 54.2 %.

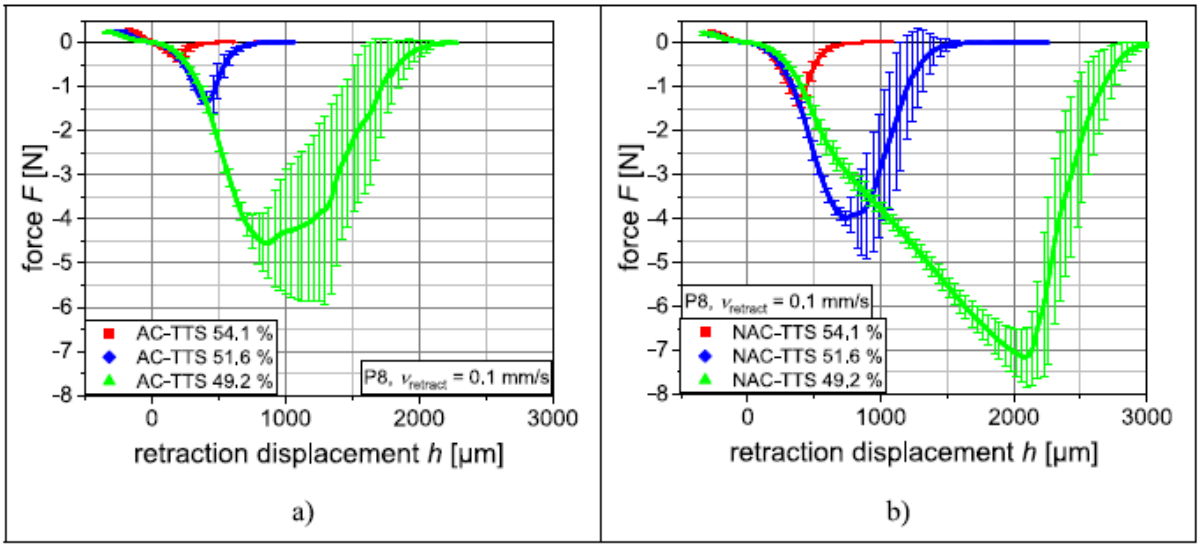

Fig. 4. Effects of chemical composition and resin content on $F-h$ curves of $AC-TTS$ (a) and $NAC-TTS$ (b) for vretract

Table 4 RheoTack quantities evaluated for rod $P8$.

		AC			NAC		
		54.2	51.6	49.1	54.2	51.6	49.1
0.01 mm/s	S (mN/mm)	804 ± 124	259 ± 81	224 ± 48	273 ± 6	247 ± 112	238 ± 31
	$h_{start\ fib}$ (µm)	151 ± 20	272 ± 31	619 ± 93	252 ± 40	730 ± 63	535 ± 61
	$F_{start\ fib}$ (N)	0.1 ± 0.0	0.3 ± 0.1	2.1 ± 0.3	0.2 ± 0.0	3.0 ± 0.3	1.5 ± 0.2
	$E_{start\ fib}$ (µJ)	9 ± 3	37 ± 9	548 ± 178	19 ± 7	754 ± 131	269 ± 53
	h_{max} (µm)	304 ± 28	809 ± 65	1752 ± 114	615 ± 52	1073 ± 116	2421 ± 264
	F_{max} (N)	0.6 ± 0.1	3.3 ± 0.2	3.6 ± 0.4	1.7 ± 0.2	3.5 ± 0.4	5.0 ± 0.3
	E_{adh} (µJ)	89 ± 22	1223 ± 102	6870 ± 215	493 ± 83	4077 ± 386	9290 ± 1077
0.1 mm/s	S (mN/mm)	1334 ± 88	610 ± 115	396 ± 69	565 ± 81	461 ± 74	431 ± 33
	$h_{start\ fib}$ (µm)	106 ± 16	150 ± 12	723 ± 63	132 ± 33	209 ± 25	649 ± 74
	$F_{start\ fib}$ (N)	0.1 ± 0.0	0.2 ± 0.0	4.0 ± 0.2	0.2 ± 0.0	0.3 ± 0.0	2.6 ± 0.2
	$E_{start\ fib}$ (µJ)	8 ± 3	18 ± 3	989 ± 158	16 ± 6	48 ± 7	551 ± 128
	h_{max} (µm)	211 ± 26	399 ± 25	898 ± 139	375 ± 29	777 ± 101	2121 ± 129
	F_{max} (N)	0.4 ± 0.1	1.4 ± 0.2	4.7 ± 0.6	1.3 ± 0.2	4.1 ± 0.2	7.3 ± 0.7
	E_{adh} (µJ)	74 ± 18	381 ± 64	4622 ± 1357	335 ± 57	2666 ± 593	10176 ± 1233
1 mm/s	S (mN/mm)	–	1085 ± 91	944 ± 52	1275 ± 67	1208 ± 83	1228 ± 45
	$h_{start\ fib}$ (µm)	–	81 ± 21	129 ± 14	–	107 ± 18	527 ± 42
	$F_{start\ fib}$ (N)	–	0.1 ± 0.0	0.2 ± 0.1	–	0.20 ± 0.06	3.0 ± 0.3
	$E_{start\ fib}$ (µJ)	–	3 ± 1	22 ± 7	–	18 ± 6	612 ± 118
	h_{max} (µm)	–	351 ± 79	550 ± 12	385 ± 28	505 ± 42	1016 ± 108
	F_{max} (N)	–	0.1 ± 0.0	2.5 ± 0.3	0.17 ± 0.03	1.9 ± 0.3	4.8 ± 0.2
	E_{adh} (µJ)	–	131 ± 74	3523 ± 866	169 ± 31	2797 ± 671	7263 ± 1190

The shapes of $F-h$-curves measured with $R5$ differed significantly from those measured with $P5$ and $P8$, except for the retraction speed of 1 mm/min. During the dwell time, sufficient adhesion was established to allow the measurement of $F-h$-curves at all three retraction speeds. $For\ AC-PSA$, the force does not decrease continuously during the detaching phase after exceeding F_{max} but stabilizes on a plateau after a sharp force drop, as shown in **Fig. 6**. In the case of $NAC-PSA$, a second force maximum occurred, **Fig. 7**.

With increasing resin content, stiffness was increased by a factor 4 at 0.01 mm/s, and a factor 2 at 0.1 mm/s and 1 mm/s for $AC-PSA$, **Table 6**. If one compares $F_{start\ fib}$, $h_{start\ fib}$, $E_{start\ fib}$, F_{max}, and h_{max} of $R5$ to those of $P5$ and $P8$, they can be considered constant with respect to STD whereas F_{max} and E_{adh} decreased one half, **Table 6**. For "softer" $NAC-PSA$ only E_{adh} exhibits a decrease to one half and the other RheoTack quantities can be considered constant with respect to STD, **Table 6**.

These results show significant changes in the PSA properties and the $F-h$-curves for resin content variations in the range of 49.1 % to 54.2 %. The $F-h$-curves reveal a strongly retraction speed-dependent detaching behavior that is affected by the conditions during the compression phase. The displacements at the end of the dwell time h_{dwell}, **Table 3**, decreased with increasing resin content due to higher PSA stiffness. Furthermore, a smaller h_{dwell} leads to smaller contact areas between the PSA and rod $R5$ but larger contact pressures. However, it lasts longer to enter the stretching and fibrillation phases for larger h_{dwell}. The compression phase becomes longer, and more time is available to establish adhesion. The total retraction speed-dependent compression time significantly exceeded a dwell time of 1 s, **Table 7**. Thus, the test conditions were not identical among $P8$, $P5$, and $R5$, although a dwell time of 1 s was chosen, as required in $ASTM$ D2979 [**33**]. To obtain identical compression times, it would be best to always retract at a constant speed until $F = 0$ and then switch to the desired retraction speed.

Obviously, the effective contact areas between the PSA and rods, as well as the gap widths, differ due to the geometries of the rods. Thus, the inclination angles of the TTS in the gap and the angles at the contact line of the PSA to the rods are retraction displacement dependent and differ for the given retraction displacements, **Fig. 8**. This has consequences for the transferred loads and stresses.

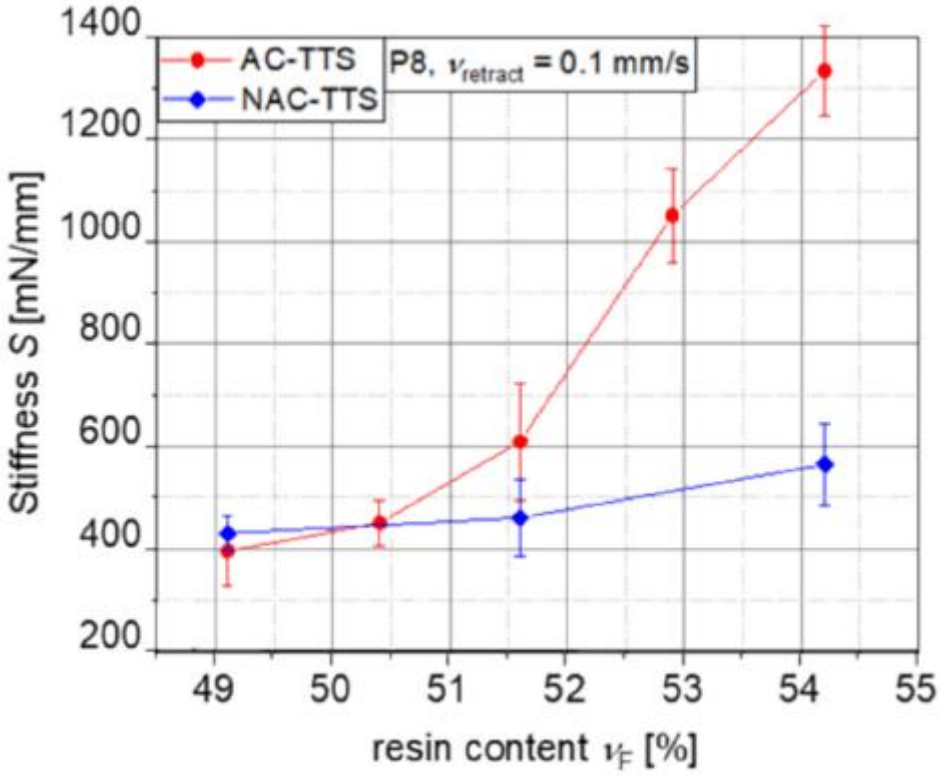

Fig. 5. Resin content dependent stiffnesses of $AC-TTS$ and $NAC-TTS$ for $v_{retract}$ = 0.1 mm/s and rod $P8$.

The stretching pattern and buckling of the TTS as a non-stiff sample were observed on the TMP as well as in the gap. This means that at a certain retraction displacement, the shear strengths of the PSA between the TMP and backing layer are exceeded, and the TTS is sliding towards the gap, **Fig. 8**. Initially, the contact areas of PSA and TMP were identical. As the load is transferred from the rod to the TMP, the shear strengths of the PSA are achieved at lower retraction displacements for $P8$ than

those for $P5$ and $R5$. **Fig. 8** also shows that after fibril formation, further retraction leads to elongation of fibrils rather than an increase in the angle of the TTS in the gap.

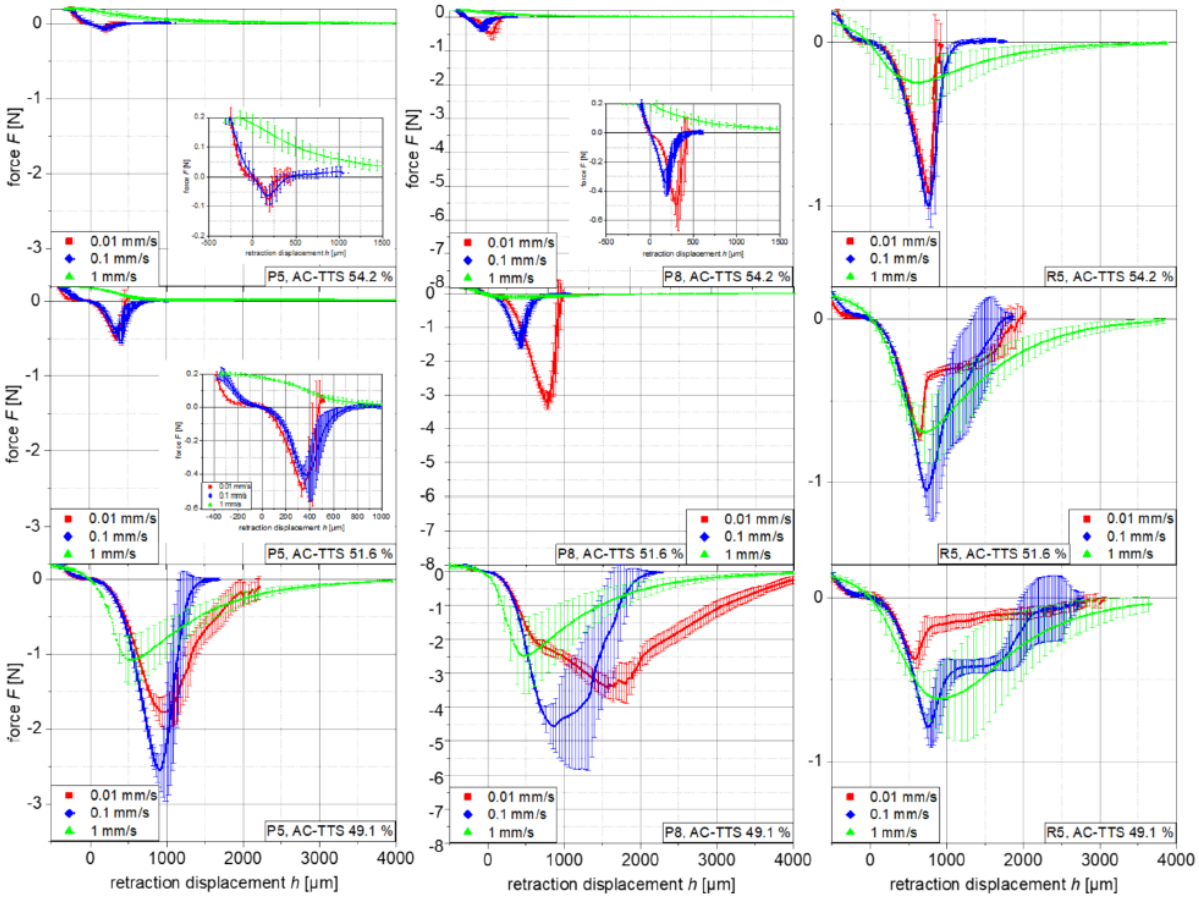

Fig. 6. Retraction speed dependent $F-h$-curves of $AC-TTS$ having resin contents of v_F = 54.2 %, 51.6 % and 49.1 % using $P5$, $P8$ and $R5$.

At a certain retraction displacement, depending on the rod geometry, the inclined TTS in the gap introduces stresses along the contact line of the PSA to the rod that exceed the shear strength of the PSA. Shear flow-induced failure starts along the contact line and propagates towards the interior of the PSA. This failure involves several steps [**40**].

If the stresses exceed the shear strength of the PSA, nanoscale cavitation is formed, which dissipates deformation energy to surface energy. Owing to the large curvature, the stresses are concentrated along the cavitation equators. PSA now has two options:

- propagation of a crack perpendicular to an external load, leading to either catastrophic cohesive failure or debonding from the rod;
- reduction of curvature and stress concentration by lengthening cavitations with subsequent formation of fibrils.

For $P5$ and $P8$ both failure types were observed. Their development depends on the resin content and retraction speed. The first fibril formation was observed along the circumferences of $P8$ and $P5$ as dot-

like structures, as shown in **Fig. 8**. Simultaneously, the contact area was reduced by partial debonding of the PSA from the rods in the order of 20 to 30 % of the cross-section visible as the blank oval area in **Fig. 8**.

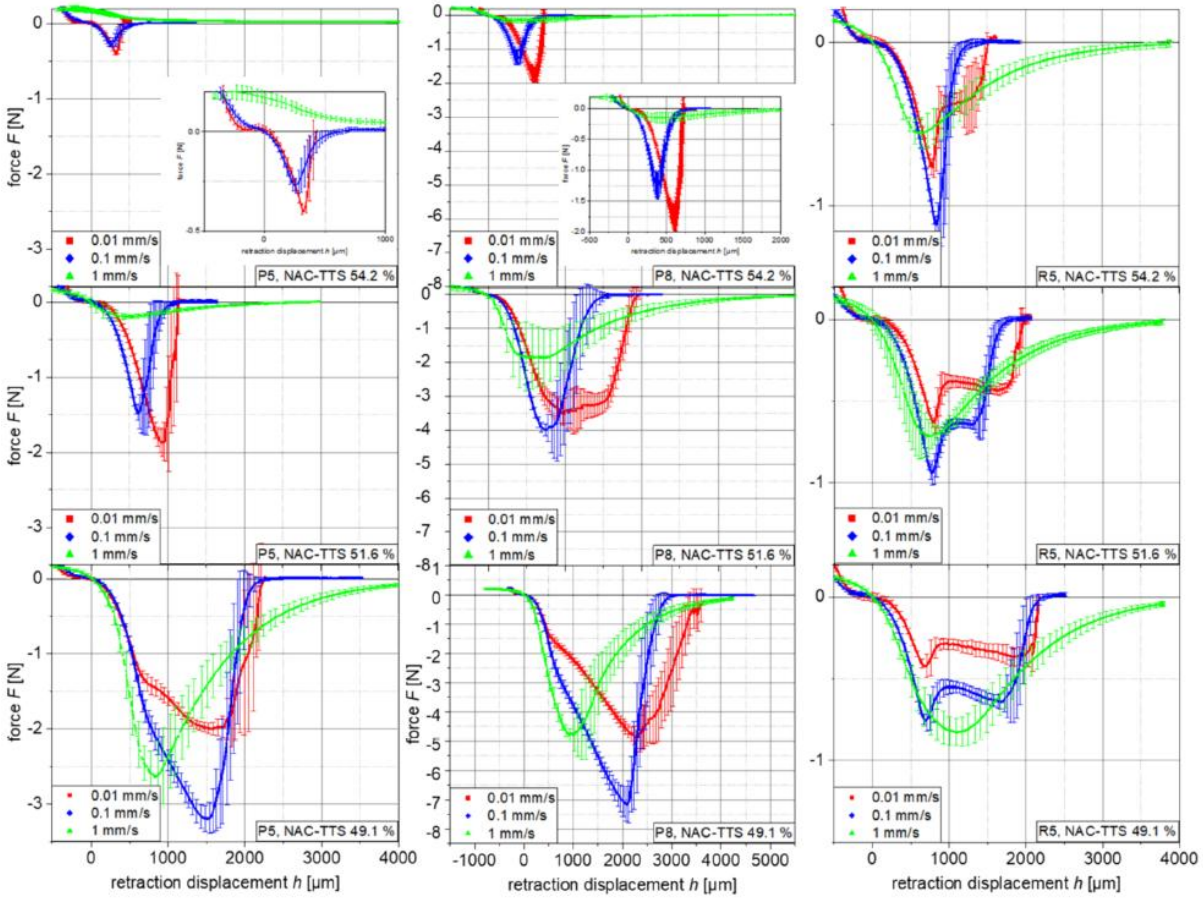

Fig. 7. Retraction speed dependent $F-h$-curves of $NAC-TTS$ having resin contents of $V_F = 54.2$ %, 51.6 % and 49.1 % using $P5$, $P8$ and $R5$.

Table 5 RheoTack parameters evaluated for rod $P5$.

		AC			NAC		
		54.2	51.6	49.1	54.2	51.6	49.1
0.01 mm/s	S (mN/mm)	418 ± 155	102 ± 31	85 ± 19	454 ± 156	112 ± 17	87 ± 15
	$h_{start\ fib}$ (µm)	87 ± 56	133 ± 21	269 ± 104	103 ± 17	337 ± 113	696 ± 102
	$F_{start\ fib}$ (N)	0.0 ± 0.0	0.1 ± 0.0	0.2 ± 0.0	0.1 ± 0.0	0.2 ± 0.0	1.3 ± 0.2
	$E_{start\ fib}$ (µJ)	3 ± 2	8 ± 3	28 ± 10	5 ± 2	26 ± 6	308 ± 69
	h_{max} (µm)	186 ± 65	374 ± 37	933 ± 141	340 ± 99	942 ± 121	1686 ± 203
	F_{max} (N)	0.1 ± 0.0	0.6 ± 0.1	1.8 ± 0.2	0.4 ± 0.0	1.9 ± 0.2	2.0 ± 0.1
	E_{adh} (µJ)	11 ± 7	107 ± 19	1551 ± 264	69 ± 8	854 ± 100	2812 ± 456
0.1 mm/s	S (mN/mm)	466 ± 70	218 ± 32	186 ± 40	463 ± 50	231 ± 44	207 ± 49
	$h_{start\ fib}$ (µm)	89 ± 29	139 ± 31	314 ± 79	93 ± 25	242 ± 68	728 ± 82
	$F_{start\ fib}$ (N)	0.0 ± 0.0	0.1 ± 0.0	0.2 ± 0.0	0.1 ± 0.0	0.2 ± 0.0	1.9 ± 0.2
	$E_{start\ fib}$ (µJ)	2 ± 1	6 ± 3	47 ± 11	3 ± 2	31 ± 6	443 ± 84
	h_{max} (µm)	176 ± 64	363 ± 44	911 ± 116	256 ± 28	646 ± 88	1493 ± 96
	F_{max} (N)	0.1 ± 0.0	0.5 ± 0.1	2.7 ± 0.2	0.3 ± 0.0	1.7 ± 0.3	3.2 ± 0.2
	E_{adh} (µJ)	12 ± 6	117 ± 29	1210 ± 585	62 ± 14	563 ± 140	3537 ± 361
1 mm/s	S (mN/mm)	–	–	665 ± 73	–	764 ± 101	696 ± 63
	$h_{start\ fib}$ (µm)	–	–	114 ± 26	–	–	218 ± 27
	$F_{start\ fib}$ (N)	–	–	0.1 ± 0.0	–	–	0.3 ± 0.1
	$E_{start\ fib}$ (µJ)	–	–	10 ± 5	–	–	43 ± 11
	h_{max} (µm)	–	–	524 ± 28	–	436 ± 43	760 ± 73
	F_{max} (N)	–	–	1.10 ± 0.38	–	0.2 ± 0.0	2.8 ± 0.4
	E_{adh} (µJ)	–	–	1152 ± 211	–	242 ± 32	3562 ± 506

Table 6 RheoTack quantities evaluated for rod $R5$.

		AC			NAC		
		54.2	51.6	49.1	54.2	51.6	49.1
0.01 mm/s	S (mN/mm)	168 ± 48	50 ± 11	30 ± 7	122 ± 16	66 ± 30	62 ± 29
	$h_{start\ fib}$ (µm)	302 ± 115	214 ± 31	239 ± 145	355 ± 149	397 ± 115	349 ± 173
	$F_{start\ fib}$ (N)	0.1 ± 0.0	0.1 ± 0.0	0.1 ± 0.0	0.1 ± 0.0	0.1 ± 0.0	0.1 ± 0.0
	$E_{start\ fib}$ (µJ)	21 ± 5	17 ± 3	8 ± 5	25 ± 7	22 ± 9	18 ± 8
	h_{max} (µm)	783 ± 109	646 ± 60	595 ± 191	764 ± 164	807 ± 137	695 ± 215
	F_{max} (N)	1.0 ± 0.1	0.7 ± 0.0	0.4 ± 0.1	0.8 ± 0.1	0.7 ± 0.1	0.5 ± 0.1
	E_{adh} (µJ)	304 ± 38	518 ± 59	350 ± 93	425 ± 66	608 ± 36	579 ± 79
0.1 mm/s	S (mN/mm)	174 ± 51	125 ± 20	97 ± 22	125 ± 20	118 ± 27	84 ± 41
	$h_{start\ fib}$ (µm)	294 ± 96	259 ± 29	296 ± 88	353 ± 99	271 ± 70	232 ± 37
	$F_{start\ fib}$ (N)	0.1 ± 0.0	0.2 ± 0.0	0.1 ± 0.0	0.1 ± 0.0	0.1 ± 0.0	0.1 ± 0.0
	$E_{start\ fib}$ (µJ)	26 ± 7	27 ± 6	21 ± 7	33 ± 6	19 ± 12	20 ± 5
	h_{max} (µm)	781 ± 106	748 ± 88	761 ± 138	858 ± 142	769 ± 86	692 ± 65
	F_{max} (N)	1.1 ± 0.1	1.2 ± 0.2	0.8 ± 0.1	1.2 ± 0.1	0.9 ± 0.1	0.8 ± 0.1
	E_{adh} (µJ)	402 ± 39	716 ± 246	812 ± 219	463 ± 77	765 ± 63	965 ± 102
1 mm/s	S (mN/mm)	524 ± 41	387 ± 28	347 ± 50	396 ± 26	467 ± 54	440 ± 76
	$h_{start\ fib}$ (µm)	115 ± 27	169 ± 29	137 ± 45	141 ± 18	152 ± 37	653 ± 69
	$F_{start\ fib}$ (N)	0.1 ± 0.0	0.1 ± 0.0	0.1 ± 0.0	0.1 ± 0.0	0.1 ± 0.0	0.6 ± 0.1
	$E_{start\ fib}$ (µJ)	5 ± 2	12 ± 6	5 ± 3	8 ± 3	11 ± 4	187 ± 34
	h_{max} (µm)	508 ± 13	643 ± 46	923 ± 188	605 ± 50	714 ± 37	1123 ± 191
	F_{max} (N)	0.3 ± 0.1	0.7 ± 0.2	0.7 ± 0.3	0.6 ± 0.1	0.7 ± 0.0	0.9 ± 0.1
	E_{adh} (µJ)	405 ± 105	953 ± 275	1064 ± 474	616 ± 291	1025 ± 88	1435 ± 151

Table 7 Retraction speed dependent compression times.

Retraction speed mm/s	Compression time s		
	P8	P5	R5
0.01	27.7	27.9	31.6
0.1	6.0	7.0	9.1
1	3.1	3.3	3.5

When the first fibrils were formed, the inclination of TTS did not change significantly. Continuing retraction led to further elongation and thinning of fibrils along the circumference until the first fibrils started to break. This occurred close to Fmax. This scenario then walks towards the inner contact areas until the PSA and rod are separated. Thus, Fmax represents a measure of fibril strength, which is governed by the retraction speed and resin content-dependent PSA moduli, fibril orientation and stretchability, PSA flowability, stress relaxation, disentangling, and strain-hardening processes [**34,53,54**].

If the load transferred from the rod to the TMP exceeds the critical force, which is the case for P5 and P8, the shear strengths of the PSA are achieved. Further rod retraction leads to shear flow in the PSA, and the backing layer slides towards the gap. The higher the transferred load, the more the TTS is shifted. Thus, hmax increased to reach F_{max}.

For $R5$, only the second option, 2, is observed, **Fig. 8**. During the dwell time, the spherical surface of $R5$ indented the PSA, similar to a hardness test with maximum stress in the center. Owing to the small compression force, the surface of $R5$ only had partial contact with the PSA. The contact area to the PSA has a diameter between 2 and 2.5 mm depending on the resin content. This small contact area confirms that the tensile forces during the detaching phase remain small enough that the shear

strength of PSA is not achieved at the interface to the TMP. The backing layer did not slide towards the gap, and TTS did not show a stretching pattern in the gap.

If $F = 0$ is achieved during retraction, the areas of the PSA along the contact circumference already experience tensile stresses, whereas the center areas are still under compression stress. Catastrophic crack propagation cannot occur under these conditions. Failure began with fibril formation along the contact circumference. At F_{max} the fibrils along the circumference started to break, and the force decreased rapidly. Subsequently, the more centrally located fibrils were stretched, which partly led to a force plateau or a second force maximum. The detaching of the PSA walks due to successive fibril stretching and breaking towards the center in an orderly manner until complete separation of PSA and $R5$. This failure behavior explains the moderate force decrease after the force drop for $AC - PSA$ and the occurrence of a second maximum force for $NAC - PSA$ during the detaching phase. This second maximum can be explained by the polar OH end groups of $NAC - PSA$, which increase the interaction of the polymer molecules and reinforce the strain hardening of the fibrils.

The inclination angle of the TTS in the gap increased with ongoing retraction. Trigonometric evaluation provided inclination angles $\alpha = 51°$, $\beta = 26°$, and $\gamma = 13°$ for $P8$, $P5$, and $R5$ at h_{max}. However, visual observation showed less inclined TTS in the gap with angles $\alpha = 36°$, $\beta = 17°$, and $\gamma = 1°$ and long vertical fibrils connecting the PSA and rod. At h_{max} the corresponding fibrils had lengths of 1 mm, 0.6 mm, and 0.57 mm, respectively. The compression stresses required to establish adhesion differ with respect to the rod geometry, as well as the compression times, **Table 7**, which depend on the resin content. This means that retraction starts from different adhesion states between the PSA and rod. In the RheoTack experiment, the 50 μm thick backing layer of the TTS represented a flexible support. This flexibility also affects the establishment of adhesion between the PSA and rods.

The consideration of the cross-sectional stress and PSA thickness in both the dwell and detaching phases at Fmax shows completely different stress and thickness situations for flat and spherical rods, **Fig. 9**.

Flat rods such as $P5$ and $P8$ have initial contact with the PSA over the complete cross-section if $h = 0$, and the PSA sticks to the rod. However, with increasing compression force, the compression stresses mainly increase along the rod edge, as the bending of the backing layer compresses the PSA in a thin circumferential stripe. The inclination of the TTS in the gap causes a clamping effect that generates a small flow of PSA towards the center, forming a rampart. The stresses in the middle of the flat rods were significantly lower than those at the edges. The consequence is an inhomogeneous cross-sectional stress field with high compression stresses along a circumferential stripe and more or less compression stress-free center areas, **Fig. 9**a. This contrasts with the commonly used rigid metal or glass substrates, which affirm a uniform cross-sectional stress field. This means that more adhesion is established during the dwell phase for $P8$ than for $P5$ because of the larger inclinations of the TTS in the gap and higher compression stresses along the circumference of P8. Thus, P8 transfers more force to the TMP, leading to more TTS sliding towards the gap and larger F_{max} and h_{max}.

The spherically rounded rod $R5$ had an initial center contact with the PSA. The flexible TTS bevels at approximately $R5$, and the compression force increases until the inclination of the TTS in the gap coincides with the tangent of the rod sphere. This generates an inhomogeneous stress field with maximum stresses in the center area and decreasing stresses towards the contact line, **Fig. 9**b. The inhomogeneous stress field has a shape similar to that generated by rigid substrates, but at a lower stress level [**55**]. The PSA experienced more compression for rigid supports than for beveled backing layers.

If the retraction reaches $h = 0$, increasing tensile stresses are introduced into the PSA for all the rods. At this moment, the backing layer bends upward in the gap, and the tensile stresses at the border of the contact area become higher than in the center owing to the notch effect, creating an inhomogeneous cross-sectional stress field, **Fig. 9**c. Further retraction leads to cavitation and subsequent fibril formation. Simultaneously, the PSA partially debonds from the flat rods in more central areas because the small pressures in the center area during the dwell phase established only little adhesion. During the ongoing retraction, the fibrils at the edges are stretched until they start to break if F_{max} is reached. This is the start for fibrils stretching towards the rod center and subsequent fibril fracture until complete failure of the PSA. The spherically rounded rod R5 also generates an inhomogeneous cross-sectional stress field, **Fig. 9**d, with the start of fibril stretching and breakage at the border of the contact area. As the center of the contact area experienced maximum compression stress in the dwell phase, the adhesion increased continuously from the border to the center. Spontaneous debonding is not possible, and fibril stretching and breakage walk towards the center.

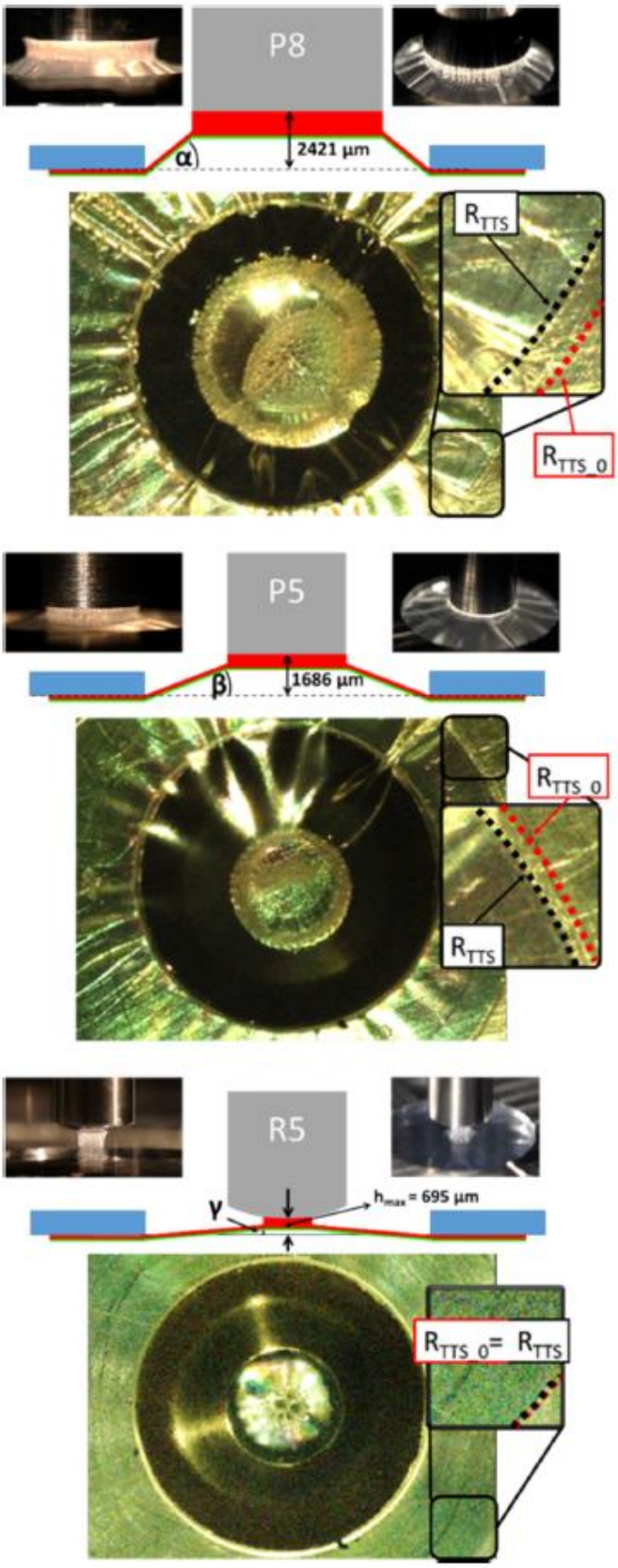

Fig. 8. Detaching situation at h_{max} for rods $P8$, $P5$, and $R5$ and corresponding pictures showing the deformation states from bottom perspective - stretching patterns of the TTS on the TMP and in the gap for $P5$ and $P8$, oval debonded areas, dot-like areas with fibrils and shifted TTS shift on TMP; from side and top perspective - stretched fibrils, and TTS inclination in the gap; $NAC - PSA$ with vf = 49.1 %, $v_{retract}$ = 0.01 mm/min.

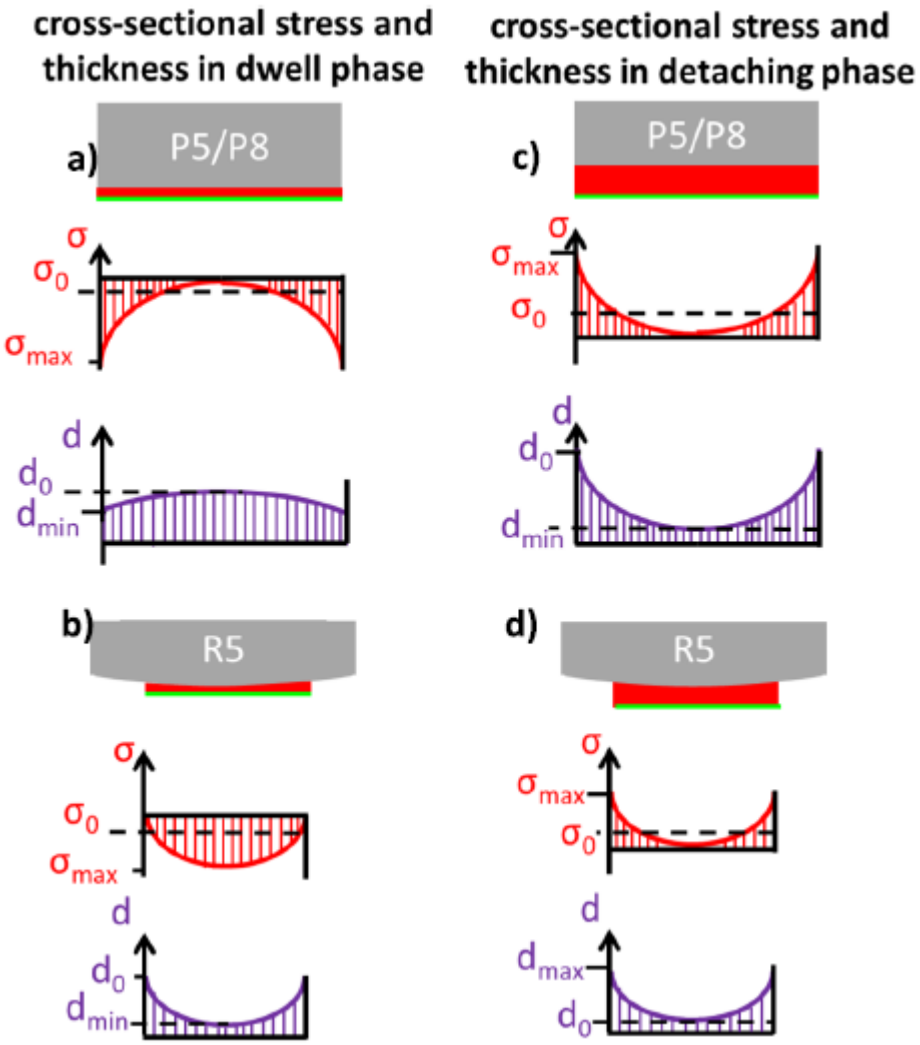

Fig. 9. Cross-sectional stress and thickness considerations of the PSA for rods $P5$ ($P8$) and $R5$ in dwell phase with ompression stresses, and in detaching phase with tensile stresses.

In addition to the effects of establishing adhesion during the compression phase, the rod geometry affected the measured magnitude of the transferred forces, **Figs. 6 and 7**. To facilitate a direct comparison, it seems reasonable to normalize the forces of $P8$ and $R5$ with respect to the cross-section of P5. If the forces are corrected using the following normalization factors:

$$n_{P8} = \frac{A_{P5}}{A_{P8}} \text{and} n_{R5} = \frac{A_{P5}}{A_{PR5}} \quad (1)$$

with the cross-sections of rods $AP5$, AP8 and $AR5$ one obtains a correspondence with $ASTM$ D2979 [**33**].

In **Fig. 10** normalized force-retraction displacement-curves are shown for $AC - PSA$ and $NAC - PSA$ with v_F = 49.1 %. The normalized force-retraction displacement curves have comparable F_{max} values for $P5$ and $P8$ at given retraction speeds and increased hmax for $P8$. The range of retraction displacements beyond hstartfib is increased for $P8$, showing that fibril formation and elongation occur over a longer time period and with lower rates as the TTS is shifted towards the gap. Furthermore, the effects of the polar OH-end groups on adhesion were clearly visible for $NAC - PSA$, as both h_{max}

and F_{max} were larger for $P8$. The determination of the contact area $R5 - PSA$ is somewhat uncertain, as the diameter of the contact area is between 2 and 2.5 mm due to optical monitoring. Thus, the normalized forces in **Fig. 10** at $R5$ were probably slightly overestimated with a diameter of 2 mm. However, the force-retraction displacement-curves exhibit similar or slightly larger F_{max} values than those of $P5$ and $P8$, and a significantly faster force increase.

Both $NAC - PSA$ and $AC - PSA$ responded in a pronounced viscoelastic manner, as shown by the retraction-rate-dependent properties, S, F_{max} and E_{adh} (**Tables 4, 5 and 6**). Silicone-based polymers and rubbers have glass transition temperatures T_g ranging —123 °C to —138 °C, respectively [**56,57**]. As the RheoTack measurements were performed at ambient temperature (23 °C), approximately 150 °C above T_g, the question arises if there are further dispersion regimes of the PSA around 23 °C, which can partly be attributed to phase transitions of the resin component.

DMA measurements using the plate-plate-arrangement clearly confirm this because they exhibit shallow and broad loss modulus (G") peaks with maxima between 0 °C and 23 °C and tanδ peaks with maxima between 40 °C and 80 °C, **Fig. 11**. This is an indication of complex PSA morphology.

The half widths of the peaks are on the order of 100 °C, indicating that the dispersion process is not a typical glass transition. Thus, both $AC - PSA$ and $NAC - PSA$ operate in the transition regime [**58**]. This explains the high rate dependent detaching behavior, as well as the rather non-sticky behavior of the PSA with v_F = 54.2 %, as the G" maximum is above the measuring temperature. The manufacturer stated that these transitions arise from the resin components. Furthermore, the tan(δ) peaks are shifted by 60 °C to 70 C° to higher temperatures compared to the G" peaks, a further statement that this is not a glass transition of a homopolymer, with shifts of typically 15 °C to 25 °C.

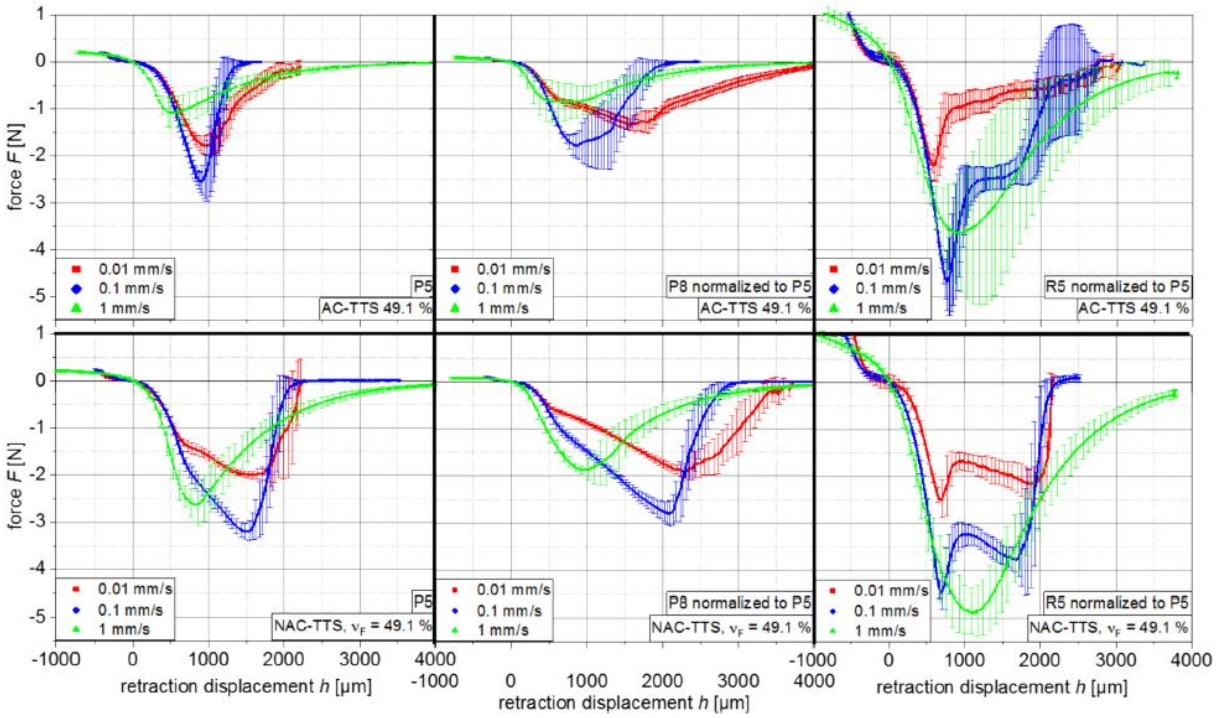

Fig. 10. Contact area normalized retraction speed dependent $F - h$-curves of $AC - TTS$ (top) and $NAC - TTS$ (bottom) with a resin content of 49.1 % investigated on $P5$, $P8$ and $R5$.

4. Conclusion

The potential of the RheoTack method was demonstrated by the investigating of the detaching behavior of silicone-based pressure-sensitive adhesives (PSA) for transdermal therapeutic systems (TTS) containing non-amine-compatible and amine-compatible PSA at practicerelevant resin contents between 49.1 % and 54.2 %. The analysis considered three retraction speeds and three rod geometries:

- retraction speeds: 0.01, 0.1 and 1 mm/s
- flat rod (D = 8 mm), flat rod (D = 5 mm), and spherical rod (D = 5 mm).

The findings can be summarized as follows:

- rod geometry directly impacts the force-retraction displacement curves and the corresponding RheoTack quantities owing to the characteristic stress and strain distributions in the compression and tensile phases;
- the normalization of forces on contact crosssections improves comparability and provides deeper insights into the deformation and failure mechanisms;
- the spherical rod produces distinct failure and detachment behavior compared to flat rods due to differences in stress and strain distributions;
- stress distribution in the PSA under the rod is essential for understanding the established adhesion states and requires further detailed stress simulation analyses, especially for flexible substrates.

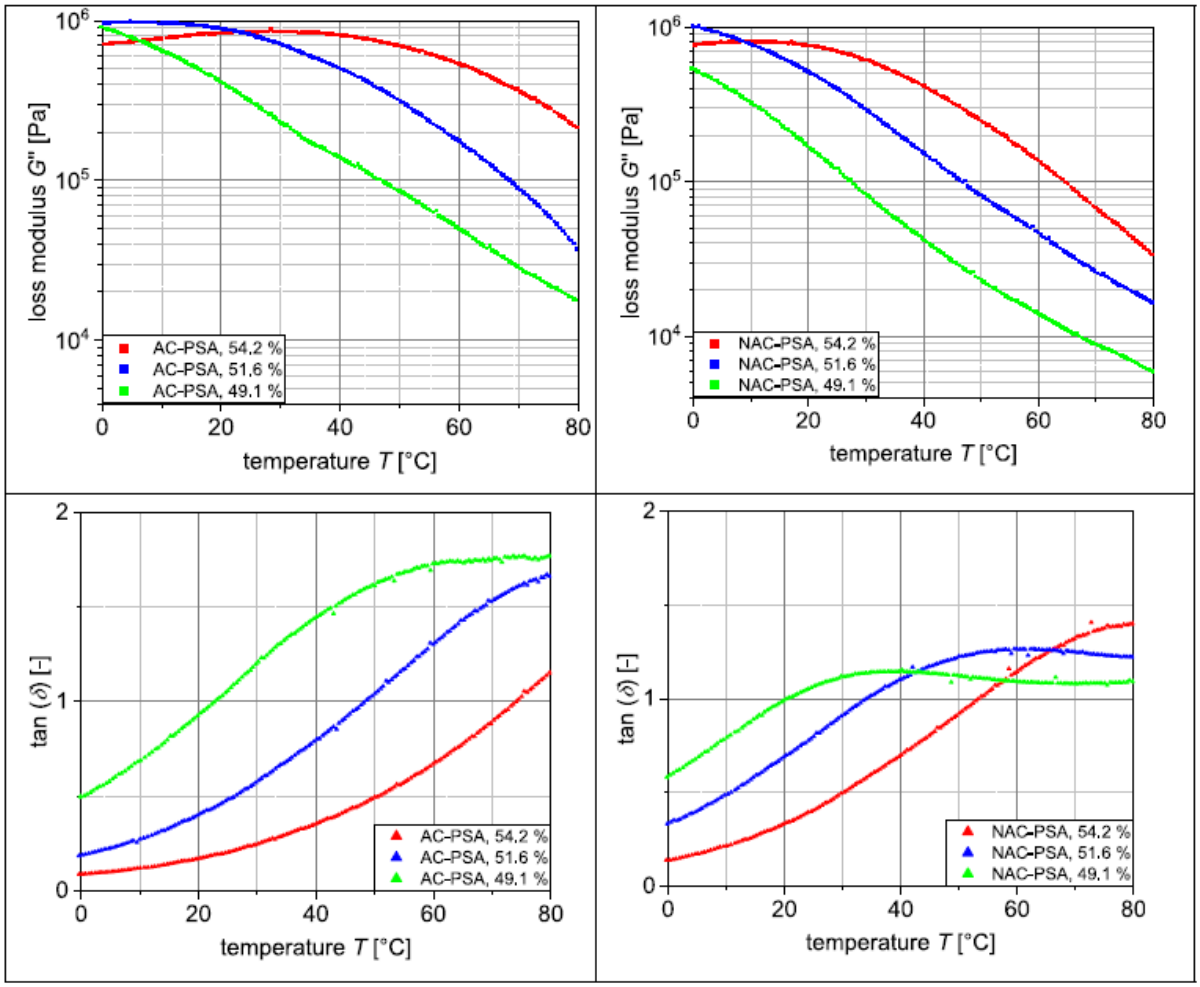

Fig. 11. Temperature and resin content dependent loss moduli G" and loss factor tan(δ) of $AC-PSA$ and $NAC-PSA$.

Impact of flexible backing layer:

- flexible backing layer as a support affects the established adhesion states during the compression phase for all the rod geometries tested;
- flexible backing layer alters adhesion and detachment behavior due to additional deformation processes: o bending of the transdermal therapeutic system (TTS) at the rod edges, causing peeling with shear stress and fibril formation o sliding of the TTS underneath the testing module;

This influence must be considered when evaluating force-retraction displacement curves to determine the failure criteria for fibril formation and detachment.

Reevaluation of dwell time and testing standards:

- the application of dwell conditions according to $ASTM$ D2979 no longer ensures comparability with previous probe tack measurements;
- in retraction speed-dependent measurements, the real dwell time consists of the total compression stress duration and depends on the retraction speed and rod geometry;

- the effects of dwell time and dwell pressure on adhesion and detaching behaviors require further study to establish a new procedure to confirm the comparability of well-defined initial adhesion states in RheoTack measurements.

This study confirmed that RheoTack is a powerful tool for the development of tailor-made PSA formulations for specific applications.

References

[1] U. S. Department of Health and Human Services Food and Drug Administration Center for Drug Evaluation and Research (CDER), Transdermal and Topical Delivery Systems - Product Development and Quality Considerations - Guidance for Industry. DOI: www.fda.gov/regulatory-information/search-fda-guidance-documents/transdermal-and-topical-delivery-systems-product-development-and-quality-considerations, 2019 (accessed 20 February 2025).

[2] P. Minghetti, F. Cilurzo, A. Casiraghi, Measuring adhesive performance in transdermal delivery systems, Am. J. Drug. Deliv 2 (2004) 193-206, **https://doi. org/10.2165/00137696-200402030-00004**.

[3] M. N. Pastore, Y. N. Kalia, M. Horstmann, M.S. Roberts, Transdermal patches: history development and pharmacology, Brit. J. Pharmacol. 172 (2015) 2179-2209, **https://doi.org/10.1111/bph.13059**.

[4] G. K. Schalau II, A. Bobenrieth, R. O. Huber, L. S. Nartker, X. Thomas, Silicone Adhesives in Medical Applications, in: H. Ozer (Ed.), Applied Adhesive Bonding in Science and Technology, London, Intech Open, 2018, pp. 93-117.

[5] S. Venkatraman, R. Gale, Skin adhesives and skin adhesion: 1. Transdermal drug delivery system, Biomaterials. 19 (1998) 1119-1136, **https://doi.org/10.1016/ S0142-9612(98)00020-9**.

[6] D. Bird, N. M. Ravindra, Transdermal drug delivery and patches - an overview, Med. Devices Sens. 3 (2022) e10069, **https://doi.org/10.1002/mds3.10069**.

[7] I. Benedek, M.M. Feldstein, Silicone Pressure-Sensitive Adhesives. Technology of Pressure-Sensitive Adhesives and Products, 2nd ed., CRC Press Taylor &Francis Group, Boca Raton, 2018, pp. 6-1 - 6-26.

[8] DuPont, Healthcare Solutions (2022) Review of silicone adhesives in healthcare applications. DuPont Healthcare Solutions. DOI: www.dupont.com/content/dam/dupont/amer/us/en/liveo/public/documents/en/16798%20Liveo%20Adhesive%20White%20Paper 06-1048-01-AGP0422.pdf, 2022 (accessed 20th February 2025).

[9] K. Ho, K. Dodou, Rheological studies on pressure-sensitive silicone adhesives and drug-in-adhesive layers as a means to characterize adhesive performance, Int. J. Pharm. 333 (2007) 24-33, **https://doi.org/10.1016/j.ijpharm.2006.09.043**.

[10] M. Meurer, R. Kádár, E. Ramakers-van Dorp, B. Möginger, B. Hausnerová, Nonlinear oscillatory shear tests of pressure-sensitive adhesives (PSAs) designed for transdermal therapeutic systems (TTS), Rheol. Acta. 60 (2021) 553-570, **https://doi.org/10.1007/s00397-021-01280-6**.

[11] C. Fang, Z. Lin, Effect of propyleneimine external cross-linker on the properties of acrylate latex pressure sensitive adhesives, Int. J. Adhes. Adhes. 61 (2015) 1-7, **https://doi.org/10.1016/j.ijadhadh.2015.04.009**.

[12] N. Karyu, K. Shitajima, S. Fujii, Y. Nakamura, Y. Urahama, Contact time dependence of tack for crosslinked polyacrylic pressure-sensitive adhesives with two different molecular structures, Int. J. Adhes. Adhes. 60 (2015) 75-82, **https:// doi.org/10.1016/j.ijadhadh.2015.04.001**.

[13] J. A. Schlademan, Tackifier Resins, in: D. Satas, Handbook of Pressure-Sensitive Adhesive Technology. (2nd ed.), Springer Science + Business Media, LLC, Berlin/ Heidelberg, 1989, pp 527-544.

[14] H. Lakrout, P. Sergot, C. Creton, Direct observation of cavitation and fibrillation in a probe tack experiment on model acrylic pressure-sensitive-adhesives, J. Adhesion. 69 (1999) 307-359, **https://doi.org/10.1080/00218469908017233**.

[15] A. Lindner, T. Maevis, T. Brummer, B. Luhmann, C. Creton, Subcritical failure of soft acrylic adhesives under tensile stress, Langmuir 20 (2004) 9156-9169, **https:// doi.org/10.1021/la049388s**.

[16] F. H. Hammond Jr., Tack, In: D. Satas, Handbook of Pressure Sensitive Adhesive Technology, (2nd ed.) Springer Science + Business Media, LLC, Berlin/Heidelberg, 1989, pp. 38-60.

[17] A. Einstein, Eine neue Bestimmung der Molekuldimensionen, Annalen der Physik 19 (1906) 289-306, **https://doi.org/10.1002/andp.19063240204**.

[18] K. Takahashi, Y. Yamagata, K. Inaba, K. Kishimoto, S. Tomioka, T. Sugizaki, Characterization of tack strength based on cavity-growth criterion, Langmuir 14 (2016) 3525-3531, **https://doi.org/10.1021/acs.langmuir.5b04705**.

[19] M. Meurer, T. Prescher, E. Ramakers-van Dorp, B. Moginger, B. Hausnerova, RheoTack-An approach to investigate retraction rate dependent detaching behavior of pressure sensitive adhesives, J. Rheol. 66 (2022) 505-513, **https://doi. org/10.1122/8.0000405**.

[20] A. Crosby, J.K.R. Shull, Adhesive failure analysis of pressure-sensitive adhesives, J. Polym. Sci. Pol. Phys. 37 (1999) 3455-3472, **https://doi.org/10.1002/(SICI) 1099-0488(19991215)37:24<3455::AID-POLB7>3.0.CO;2-3**.

[21] A.E. ÓConnor, N. Willenbacher, The effect of molecular weight and temperature on tack properties of model polyisobutylenes, Int. J. Adhes. Adhes. 24 (4) (2004) 335-346, **https://doi.org/10.1016/j.ijadhadh.2003.11.005**.

[22] M.M. Feldstein, R.A. Siegel, Molecular and nanoscale factors governing pressure-sensitive adhesion strength of viscoelastic polymers, J. Polym. Sci. Pol. Phys. 50 (2012) 739-772, **https://doi.org/10.1002/polb.23065**.

[23] C. Creton, L. Leibler, How does tack depend on time of contact and contact pressure? J. Polym. Sci. Pol. Phys.3 34 (1996) 545-554, **https://doi.org/10.1002/(SICI)1099-0488(199602)34:3<545::AID-POLB13>3.0.CO;2-I**.

[24] E. Maurer, S. Loi, D. Wulff, N. Willenbacher, P. Muller-Buschbaum, Microscopic structure in pressure sensitive adhesives: an ultrasmall angle X-ray study, Phys. B 357 (2005) 144-147, **https://doi.org/10.1016/j.physb:2004.11.044**.

[25] J. Nase, Debonding of viscoelastic materials: from a viscous liquid to a soft elastic solid (Dissertation, Saarland University, 2009).

[26] P. Tordjeman, E. Papon, J.-J. Villenave, Tack properties of pressure-sensitive adhesives, J. Polym. Sci. Pol 38 (2000) 1201-1208, **https://doi.org/10.1002/(SICI)1099-0488(20000501)38:9<1201::AID-POLB12>3.0.CO;2-#**.

[27] K. Brown, J.C. Hooker, C. Creton, Micromechanisms of tack of soft adhesives based on styrenic block copolymers, Macromol. Mater. Eng. 287 (2002) 163-179**, https://doi.org/10.1002/1439-2054(20020301)287:3<163::AID-MAME163>3.0. CO;2-P**.

[28] TA Instruments, Pressure-Sensitive Adhesive Tack Using the ARES Rheometer. DOI: www.tainstruments.com/pdf/literature/L2084 Tack Testing ARES.pdf, 1999 (accessed 20th February 2025).

[29] Malvern Instruments, Application Note: Assessing tackiness and adhesion using a pull away test on a rotational rheometer. DOI:cdn.technologynetworks.com/TN/ Resources/PDF/AN150527AssessingTackinessPullAway.pdf, 2015 (accessed 20th February 2025).

[30] NETZSCH Geroatebau GmbH, Application note: Determination of Pressure-Sensitive Tack and Adhesion Using Axial Measurements on a Rotational Rheometer - Blu-Tack®. www.netzsch.com, 2022 (accessed 20th February 2025).

[31] TA Instruments, Application note: Rheological Analysis of Tack, http://www. tainstruments.com/pdf/literature/AAN018 V1 Analysis%20of%20tack.pdf, 2021 (accessed 20th February 2025).

[32] Anton Paar, Application note: Combined rheological methods: from Rheo-optics to magneto-rheology and beyond, DOI: www.anton-paar.com, 2021 (accessed 20th February 2025).

[33] American Society for Testing and Materials (ASTM), Standard Test Method for Pressure-Sensitive Tack of Adhesive Using an Inverted Probe Machine - ASTM D2979 (ASTM International, West Conshohocken, 2016), Vol. 15.10.

[34] K. Takahashi, O. Ryuto, K. Inaba, K. Kishimoto, Scaling effect on the detachment of pressure-sensitive adhesives through fibrillation characterized by a probe-tack test, Soft Matter 16 (2020) 6493-6500, **https://doi.org/10.1039/D0SM00680G**.

[35] S. Moon, A. Chiche, A.M. Forster, W. Zhang, C.M. Stafford, Evaluation of temperature-dependent adhesive performance via combinatorial probe tack measurements, Rev. Sci. Instrum. 76 (2005) 062210-062211, **https://doi.org/ 10.1063/1.1906105**.

[36] S. Mehravar, N. Ballard, A. Agirre, R. Tomovska, J.M. Asua, Relating polymer microstructure to adhesive performance in blends of hybrid polyurethane / acrylic latexes, Eur. Polym. J. 87 (2017) 300-307, **https://doi.org/10.1016/j. eurpolymj.2016.12.031**.

[37] A. Zosel, Adhesion and tack of polymers: Influence of mechanical properties and surface tensions, Colloid. Polym. Sci. 263 (1985) 541-553, **https://doi.org/10.1007/BF01421887**.

[38] A. Zosel, Adhesive failure and deformation behavior of polymers, J. Adhesion. 30 (1989) 135-149, **https://doi.org/10.1080/00218468908048202**.

[39] S.B. Lin, Silicone pressure-sensitive adhesives with selective adhesion characteristics, J. Adhes. Sci. Technol. 10 (1996) 559-571, **https://doi.org/10.1163/156856196X00580**.

[40] C. Creton, M. Cicotti, Fracture and adhesion of soft materials, Rep. Prog. Phys. 79 (2016) 046601. DOI: hal.archives-ouvertes.fr/hal-01436885.

[41] C. Creton, H. Lakrout, Micromechanics of flat-probe adhesion tests of soft viscoelastic polymer films, J. Polym. Sci. Pol. Phys. 38 (2000) 965-979, **https://doi.org/10.1002/(SICI)1099-0488(20000401)38:7<965::AID-POLB7>3.0.CO;2-8**.

[42] E. Gutschke, S. Bracht, S. Nagel, W. Weitschies, Adhesion testing of transdermal matrix patches with a probe tack test - In vitro and in vivo evaluation, Eur. J. Pharm. Biopharm. 75 (2010) 399-404, **https://doi.org/10.1016/j. ejpb.2010.03.016**.

[43] A. Chiche, P. Pareige, C. Creton, Role of surface roughness in controlling the adhesion of a soft adhesive on a hard surface, C. R. Acad- Sci. Paris. 1 (2000) 1197-1204, **https://doi.org/10.1016/S1296-2147(00)01133-1**.

[44] R. Deblieck, D.J.M. van Beek, K. Remerie, I.M. Ward, Failure mechanism in polyolefins: The role of crazing, shear yielding and the entanglement network, Polymer 52 (2011) 2979-2990, **https://doi.org/10.10Wj.polymer.20n.03.055**.

[45] R. Estevez, M.G.A. Tijssens, E. Van der Giessen, Modelling of the competition between shear yielding and crazing in glassy polymers, J. Mech. Phys. Solids. 48 (2000) 2585-2617, **https://doi.org/10.1016/S0022-5096(00)00016-8**.

[46] J.P. Manaia, F.A. Pires, A.M.P. Jesus, Elastoplastic and fracture behavior of semicrystalline polymers under multiaxial stress states, Fracture and Structural Integrity. 47 (2019) 82-103, **https://doi.org/10.3221/IGF-ESIS.47.08**.

[47] S. Basu, D.K. Mahajan, E. Van der Giessen, Micromechanics of the growth of craze fibril in glassy polymers, Polymer 46 (2005) 7504-7518, **https://doi.org/10.1016/ j.polymer.2005.05.148**.

[48] DuPont, Liveo™ BIO-PSA 7-4201 silicone adhesives, DuPont. DOI:dupont. materialdatacenter.com/gb/products/pdf/SI/Liveo%E2%84%A2%20BIO-PSA%207-4201-gb.pdf, 2021 (accessed 20th'February 2025).

[49] DuPont, Liveo™ BIO-PSA 7-4301 silicone adhesives, DuPont. DOI:dupont. materialdatacenter.com/gb/products/pdf/SI/Liveo%E2%84%A2%20BIO-PSA%207-4301-gb.pdf, 2021 (accessed 20th'February 2025).

[50] DuPont, Liveo™ BIO-PSA 7-4501 silicone adhesives, DuPont. DOI:dupont. materialdatacenter.com/gb/products/pdf/SI/Liveo%E2%84%A2%20BIO-PSA%207-4501-gb.pdf, 2021 (accessed 20th'February 2025).

[51] DuPont, Liveo™ BIO-PSA 7-4601 silicone adhesives, DuPont. DOI:dupont. materialdatacenter.com/gb/products/pdf/SI/Liveo%E2%84%A2%20BIO-PSA%207-4601-gb.pdf, 2021 (accessed 20th'February 2025).

[52] Mtm, Scotchpack™, Polyester Backing Film Laminate. DOI:www.solventum.com/en-us/home/f/b0004241/, 2024 (accessed 20th February 2025).

[53] M.A. Droesbeke, A. Simula, J.M. Asua, F.E. Du Prez, Biosourced terpenoids for the development of sustainable acrylic pressure-sensitive adhesives via emulsion polymerization, Green Chem. 22 (2020) 4561, **https://doi.org/10.1039/ D0GC01350A**.

[54] K. Takahashi, M. Shimizu, K. Inaba, K. Kishimoto, Y. Inao, T. Sugizaki, Tack performance of pressure-sensitive adhesive tapes under tensile loading, Int. J. Adhes. Adhes. 45 (2013) 90-97, **https://doi.org/10.1016/j.ijadhadh.2013.05.005**.

[55] A.C. Fisher-Cripps, Nanoindentation, Springer Science + Business Media, Berlin/Heidelberg, 2011.

[56] K. Zalewski, Z. Chylek, W.A. Trzcmski, A review of polysiloxanes in terms of their application in explosives, Polymers 13 (2021) 1080, **https://doi.org/10.3390/ polym13071080**.

[57] Hitachi High-Tech Science Cooperation, Thermal Analysis of Silicone Rubber. DOI: www.hitachi-hightech.com/file/global/pdf/products/science/appli/ana/thermal/application TA 018e.pdf, 1985 (accessed 20t February 2025).

[58] T. Mezger, Das Rheologie Handbuch, Vincentz Network, Hannover, 2012.